Materials Today: Proceedings xxx (xxxx) xxx

Contents lists available at ScienceDirect

Materials Today: Proceedings

journal homepage: www.elsevier.com/locate/matpr

Role of Mo in the nucleation of intermetallic laves phase

S. Kumar [a], S. Sirohi [a,*], J.G. Thakare [b], B. Adhithan [a], C. Pandey [c]

[a] SRM Institute of Science and Technology Delhi NCR Campus Modinagar, UttarPradesh 201204, India
[b] School of Mechanical Engineering, VIT Vellore, Chennai, India
[c] Department of Mechanical Engineering, IIT Jodhpur, Rajasthan 342037, India

ARTICLE INFO

Article history:
Received 24 June 2020
Received in revised form 17 August 2020
Accepted 28 August 2020
Available online xxxx

Keywords:
P91
Laves phase
Creep
PWNT
SMAW
GTAW

ABSTRACT

The present research work investigates the effect of the re-austenitizing based post-welded tempering (PWNT) treatment on microstructure evolution and fracture characteristics of the P91 welds joint under creep exposure condition. The major problem associated with the P91 welded joint is the failure from the soft inter-critical heat affected zone (ICHAZ) during elevated creep service conditions. The failure is associated with the altering of the microstructure of the P91 steel as a result of the welding heat, which leads to the formation of ICHAZ. To investigate the creep performance of the welded joint, creep tests have been conducted at 620 °C for applied stress of 200 MPa (PWNT 1) and 150 MPa (PWNT 2). The crept specimen was carried out in detail by using the scanning electron microscope (SEM). The PWNT have observed a significant effect on fracture characteristic, and it shifted from the soft ICHAZ to over-tempered base zone. The inter-metallic Laves phase was observed in each region of the weldments for specimen exposed at 620 °C for applied stress of 150 MPa (PWNT 2).

1. Introduction

The continuous consumption of fossil fuels in coal-fired power plants leads to environmental pollution through the emission of greenhouse gases [1,2]. To protect the environment from the gaseous pollution and enhance the efficiency of the plants, ultra-supercritical (USC) power plants are constructed. The aim of poor pollution and enhanced efficiency is achieved by increasing the operating parameters of steam [3–5]. The traditional creep strength enhanced martensitic steel like P122 is not used in such conditions as a result of poor oxidation resistance [6,7]. To meet the challenges, 9% Cr steel is developed with excellent creep-rupture properties and oxidation resistance at a higher temperature of about 600–650 °C [8–10]. At the initial stage of the development of the 9% Cr steel, P9 steel was developed. P91 steel has been developed by adding the micro-alloying element like V, Nb, and N in P9 steel with enhancing creep strength and mechanical properties [11–13]. A lot of studies have been conducted to investigate the effect of heat treatment on microstructure and mechanical behavior of the P91 steel and their weldments [14–18]. The P91 steel weldments have reported a serious issue during the elevated temperature service application-because of the common failure of the steam generator components from the welds joint. The failure of the welded jointmost commonly occurred in the soft fine-grained heat-affected (HAZ) or inter-critical HAZ [19–22], and termed as the Type IV failure. The failure associated with soft ICHAZ/FGHAZ zone resulted in inferior creep properties of the P91 welds joint as compared to virgin P91 steel. A lot of trial basis heat treatments were performed to enhance the elevated temperature strength of P91 welds joint and to overcome the Type IV cracking [23–25]. The most common heat treatment employed for martensitic grade welds joint istempering in the temperature range of 730–760 °C for the varying time in the range of 60–120 mins [26,27].The studies related to re-austenitizing based post-weld tempering (PWNT) treatment has also been performed for the P91 welded joint and have observed a positive response on mechanical and microstructural behavior [15].The PWNT also helps in the dissolution of unwanted delta ferrite patches forms in WM and HAZ during the welding cycle [28,29]. The hydrogen induced cold cracking of the welds joint is

* Corresponding author.
E-mail addresses: sachinsirohi2008@gmail.com (S. Sirohi), jayantgopal.thakare@vit.ac.in (J.G. Thakare).

https://doi.org/10.1016/j.matpr.2020.08.734
2214-7853/

another serious issue. Schaupp et al. [30] had performed the Weldability test of the 960 MPa grade high-strength steels by using the Implant test. The effect of the diffusible hydrogen content on lower critical stress has also been studied. The crack initiation during the implant tests was mainly observed in coarse-grained HAZ because of their brittle nature. The brittleness nature in CGHAZ can be reduced by using the reasonable bead.

Sequence [31]. Pandey et al.[32,33] had also studied the role of the diffusible hydrogen content on mechanical performance of the welds joint by using the Implant tests. The mechanical properties of the welds joint get decreased significantly by increasing the amount of the diffusible hydrogen content in the deposited metal.

From literature, it is clear that the research related to the effect of the PWNT on creep behaviors of the P91 welded joint has not been reported yet. The present work focuses on the creep behavior of the P91 welded joint and microstructure characterization of WM and HAZ for the crept specimen.

2. Experimental details

The P91 steel plate of dimensions 150 mm × 100 mm × 18mmwas used for the experiment purpose. The joining of the P91 steel plate was carried out by using the shielded metal arc welding (SMAW) process and Gas Tungsten Arc (GTA) welding process. The detailed experimental investigation, including the welding process parameters and groove designs are discussed in my earlier work [34]. TheGTA welding process with ER90S-B9electrode(Φ1.6 mm) and SMAW processwith electrode rod of diameter 4 mm wasemployed for the root passes and filling passes, respectively. The welded jointhas been subjected to re-austenitizing at 1040 °C for 60 min and followed bytempering at 760 °C for 2 h (PWNT) [35,36].The creep test specimens were machined from the heat-treated plate with gauge length and gauge diameter of 50 mm and 4 mm, respectively, as per reference [36]. The test condition employed for the creep is depicted in Table 1. The crept specimen has been cross-sectioned for the metallographic characterization and mounted in resin. For polishing, standard metallography technique has been utilized. To reveal the microstructure of the different zone in the crept specimen, polished samples were etched in Villella's solution. The fracture surface of the crept samples was also studied using the optical microscope. The creep curves for PWNT 1 and PWNT 2 are discussed in my previous work [34]. The creep rupture life is measured to be 467 hrs for PWNT 1 condition and 2432 hrs for PWNT 2 condition.

Table 1
Creep tests condition.

Creep test condition	Applied stress (MPa)	Temperature (°C)	Fracture location
PWNT 1	200	620	BM
PWNT 1	150	620	BM

3. Results and discussion

3.1. Microstructure evolution during the creep exposure

The crept specimen for both the heat-treatment conditions is depicted in Fig. 1(a). For microstructure characterization in a different zone and to serve the fracture location, the fractured specimens are mounted in resin, as shown in Fig. 1(b). Fig. 1(b) shows the fracture location of the creep tested specimen, and it was in over-tempered base zone. The weld zone, HAZ, and over-tempered base zone are clearly marked in Fig. 1(b). The detailed characterization of different zones (pointed in Fig. 1(b)) of the fractured specimen is discussed below.

Fig. 2 shows the micrograph of the crept sample at different locations for both PWNT 1 and PWNT 2 conditions. For PWNT 1, the creep cavities are observed near the crack tip of the fractured specimen, as depicted in Fig. 2(a). At the AGBs, a higher density of the coarse carbide particles is observed in the black dotted form (Fig. 2(a)). The creep cavities are mainly noticed along the lath

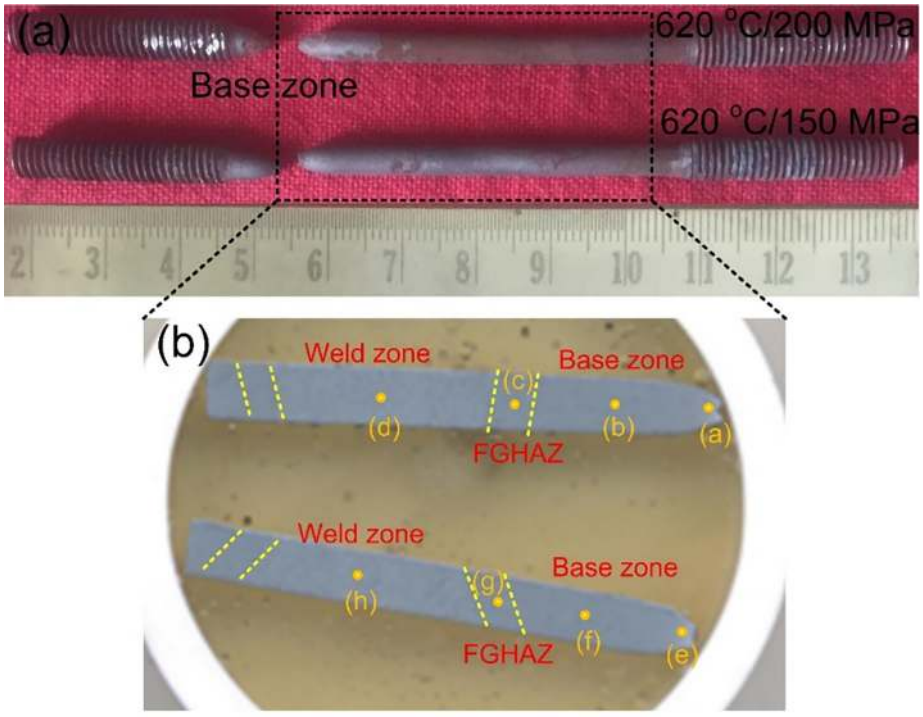

Fig. 1. (a) Fractured creep tests specimen in different PWNT condition (b) mounted specimen removed from the crept specimen for detail microstructure analysis.

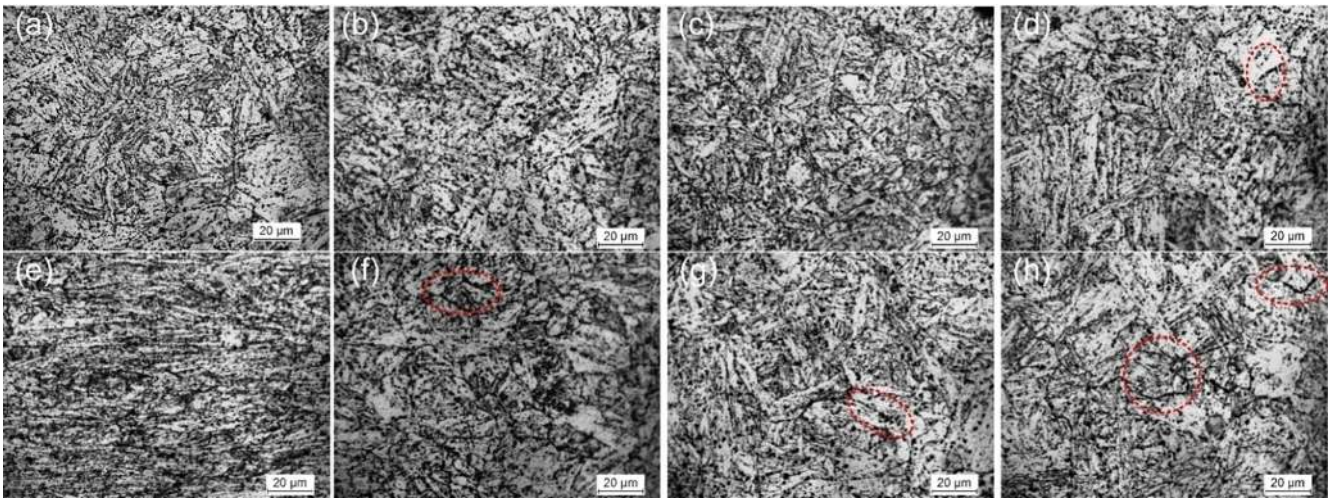

Fig. 2. Micrographs at different locations, as shown in Fig. 3(b); for PWNT 1 (a) at crack tip, (b) away from crack tip, (c) fine-grained HAZ, (d) WFZ; for PWNT 2 (e) at crack tip, (f) away from crack tip, (g) FGHAZ, (h) WFZ.

blocks and PAGBs and formation of creep cavities are attributed to the evolution of the brittle intermetallic phases and presence of coarse $M_{23}C_6$ particles. The lath blocks surrounded by the precipitates are also observed inside the packet boundaries of the PAGBs. The precipitates located along the boundaries show the brittle nature as compared to the martensitic matrix. At point b (Fig. 2(b)), the density of particles is higher, and the PAGBs are also difficult to trace that confirms the coarsening of the grains. The microstructure observed at point c (FGHAZ) shows a similar behavior as point a. Both PAGBs and lath blocks are observed to be surrounded by the precipitates, as depicted in Fig. 2(c). However, the density of coarse precipitates is observed to be less as compared to point b. The identical microstructure with almost similar grain size, precipitate size, and hardness was reported for the PWNT specimen [14,37]. However, the size of precipitates and the size of grains after he PWNT are observed to be much higher than the post-weld heat-treated sample and as-received material [9,11]. The coarse precipitates present in P91 weldments undergo further coarsening during the creep exposure that results in the formation of deep cavities. The microstructure at point d (fusion zone) shows the presence of tempered martensite with coarse precipitates. In the weld fusion zone, coarse precipitates along the PAGBs are shown in the red circle of Fig. 2(d).

For PWNT 2, the micrograph at a different location is shown in Fig. 2(e–h) as per Fig. 1(b) [38]. The characterization of the crept sample for the PWNT 2 condition is taken from my previous work [38]. At point e, elongated lath blocks are observed in the direction of the loading along with minute creep cavities (Fig. 2(e)). For PWNT 2, the density of the coarse precipitates is observed higher than the PWNT 1. The precipitates in the lower stress regime are confirmed as the coarse $M_{23}C_6$ and intermetallic Laves phase. The Mo-rich Laves phase (Fe_2Mo) is developed during creep exposure.

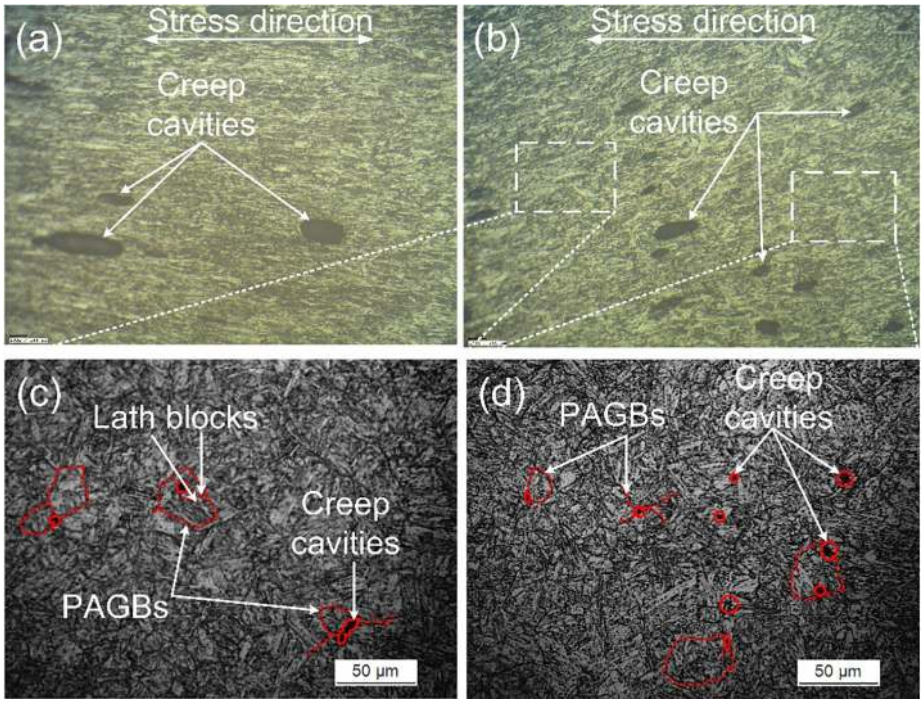

Fig. 3. Micrographs of crack tip (a) creep sample for PWNT 1, (b) creep sample PWNT 2; magnified view showing location of the cavities for (c) PWNT 1, (d) PWNT 2.

The accumulation of the coarse precipitates in the subzone of the crept P91 welded sample is highlighted in the red circle. At point f and g (FGHAZ), the coarse PAGBs are difficult to observe, and it can be traced by the precipitates present along it, as shown in Fig. 2(f) and 2(h), respectively. For short term creep exposure, both $M_{23}C_6$ and Laves phase provide the pinning to grain boundaries and improves the strength of the welds joint. The Laves phase shows a higher coarsening rate after the evolution [6,39,40] and losses their pinning effect with time. In WFZ (point h), grain boundaries are clearly traceable by the precipitates (Fig. 2(h)).

For further investigation of the crack tip, the low magnification optical micrographs are taken, as shown in Fig. 3. For the creep exposed sample at 620 °C at 200 MPa (PWNT 1), the crack tip of the crept sample shows the elongated deep cavities in the direction of the loading, as shown in Fig. 3(a-b). However, a number density of creep cavities for PWNT 2, i.e., the low level of applied stress was measured higher as compared to PWNT 1, as shown in Fig. 3(b). The detailed view of crack-tip shows the origin of the creep cavities, and it was generally originated at the PAGBs or along the lath blocks having a higher density of the precipitates, as shown in Fig. 3(c–d). The nucleation of the creep cavities along the PAGBs and lath blocks leads to higher stress concentration as a result of brittle, coarse precipitates, and soft matrix. The creep voids are generally considered along the packet boundaries, lath boundaries, PAGBs, or triple boundaries, mainly due to a higher density of secondary phase coarse $M_{23}C_6$ particles or Laves phase. The voids formation at the triple boundaries of PAGBs and martensite laths are clearly shown in Fig. 3(c). The stress concentration as a result of coarse precipitates is widely accepted and reported cause of creep voids/creep cavities resulting in final creep fracture of the P91 welded joint [41].

Typical SE image at different zone of the crept specimen is shown in Fig. 4 for both low and high applied stress regimes at creep exposure temperature of 620 °C. For PWNT 1 condition, at

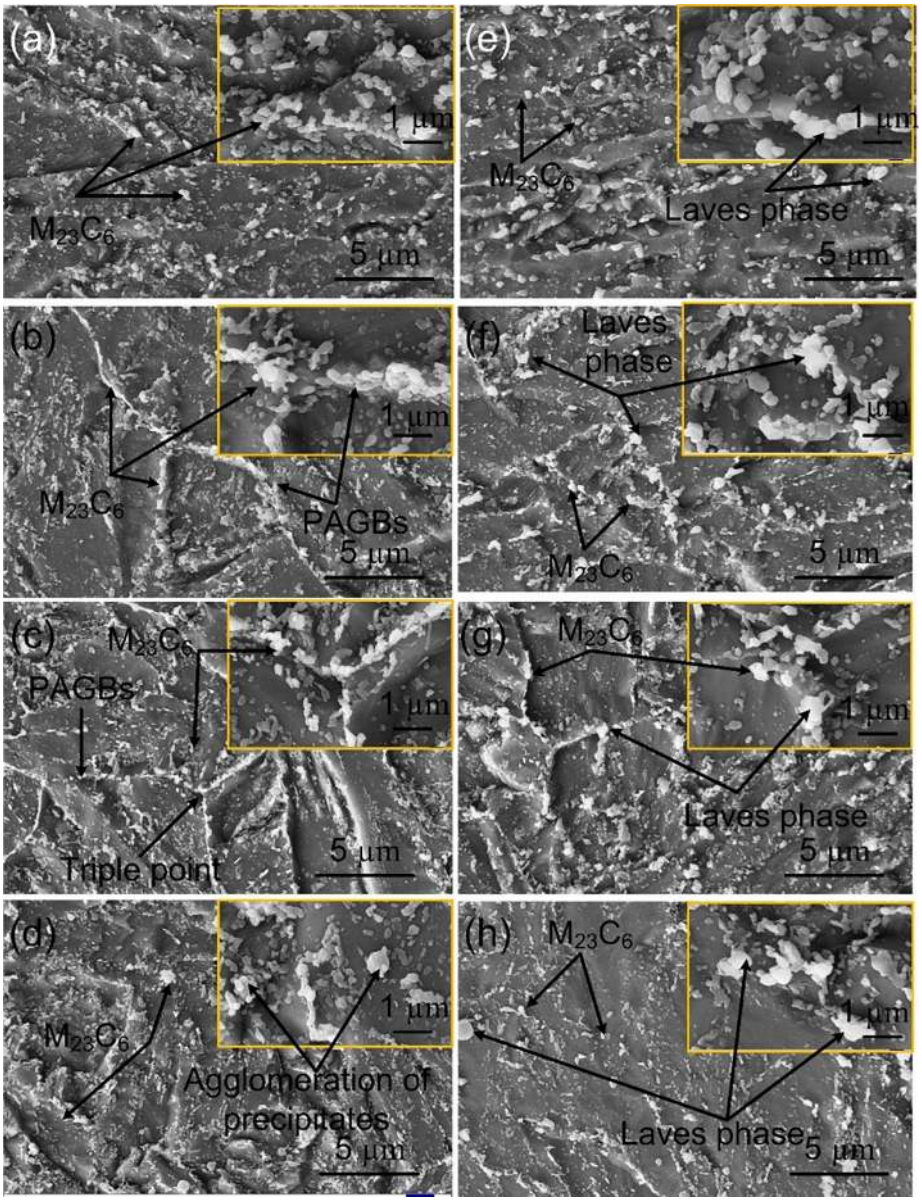

Fig. 4. Micrographs at different location as shown in Fig. 1(b); for PWNT 1 (a) at crack tip, (b) away from crack tip, (c) FGHAZ, (d) WFZ; for PWNT 2 (e) at crack tip, (f) away from crack tip, (g) FGHAZ, (h) WFZ.

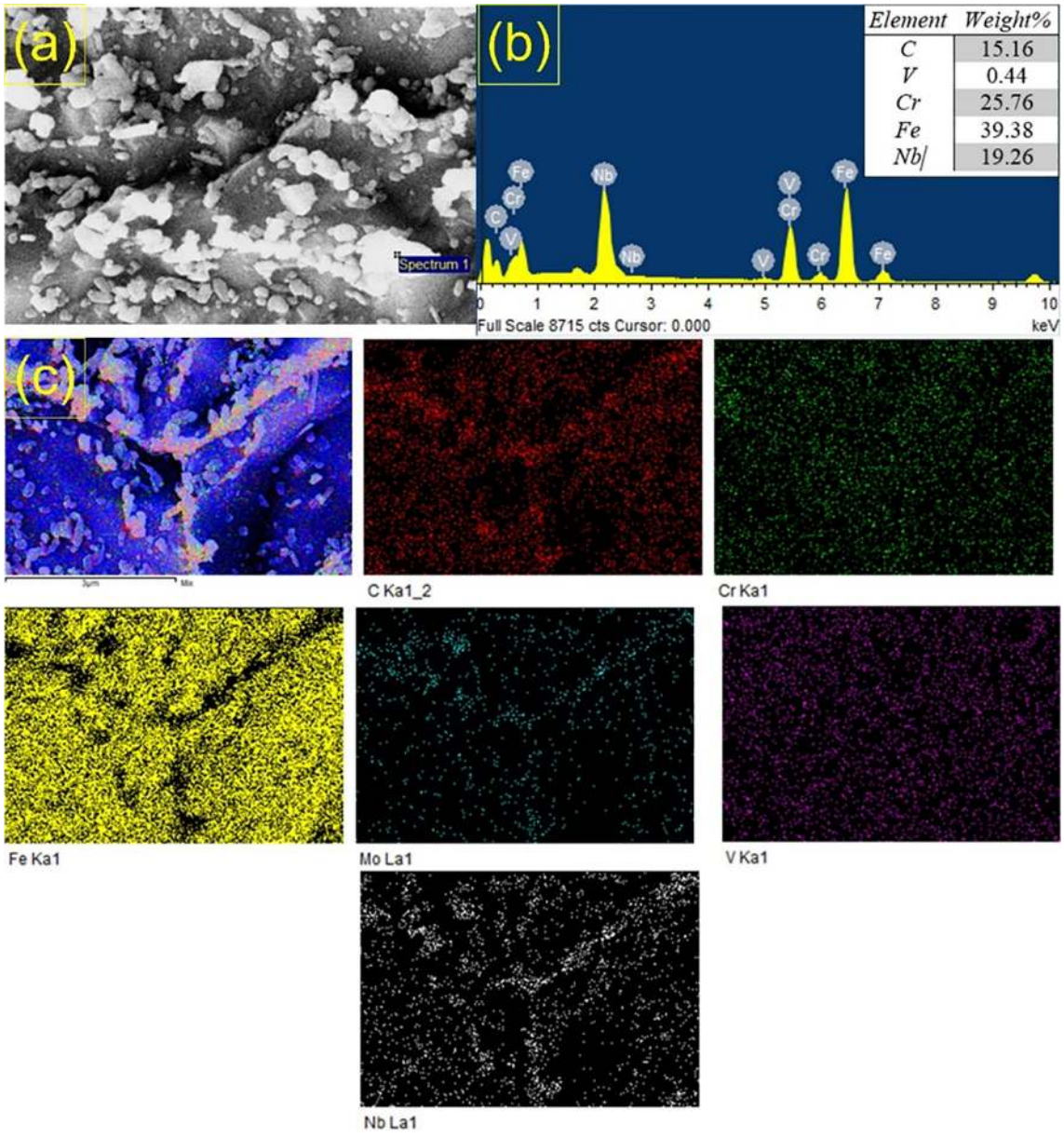

Fig. 5. Higher magnification micrograph at the crack tip for crept specimen of PWNT 1 condition, (b) EDS analysis of the white particles located at PAGBs, (c) area elemental mapping of the FGHAZ for PWNT 1 condition.

crack tip (point a), typical columnar lath decorated with coarse precipitates are observed, as shown in Fig. 4(a). Typical size and morphology of coarse $M_{23}C_6$ precipitates are shown in the top right portion of Fig. 4(a). At point b, microstructure looks similar to point a with coarse $M_{23}C_6$precipitates along lath and PAGBs. The coarse precipitates density is observed higher at PAGBs and lath blocks, as shown in Fig. 4(b). The fine precipitates in order of 20–40 nm are observed inside the martensitic matrix region and remain stable thought out the creep exposure service, confirmed as V and Nb-rich MX type precipitates [42]. In FGHAZ (point c), triple point with a higher density of precipitates is observed that resulted in higher stress concentration at triple points, which leads to damage. The triple point with a higher density of the precipitates is also observed in Fig. 4(c). At point d (WFZ), microstructure looks different as compared to other points in terms of precipitates morphology. In micrograph of the WFZ shows the agglomeration of carbide precipitates at the grain boundaries (Fig. 4(d)). The size of the agglomerated precipitates measured to be in the range of 490–600 nm.The agglomeration of precipitates also leads to stress concentration and leading to crack nucleation.

The micrograph of the different zone in PWNT 2 conditions (620 °C/150 MPa) is shown in Fig. 4(e–h) and includes the crack tip, base zone, FGHAZ, and WFZ [38]. The characterization of the crept sample in the PWNT 2 condition is reported in detail in my previous work [38]. At point (e), typical elongated columnar lath morphology is observed. The coarse precipitates which are surrounded by some other fine precipitates are observed in the crack tip zone, as shown in Fig. 4(e). For detailed observation, the SE micrograph at a magnification of 50000x is taken, as shown in the top right of Fig. 4(e). The SE image shows the accumulation of precipitates at the grain boundaries and lath blocks. The Laves phase (Fe_2Mo) evolution is observed in each zone of the PWNT 2 crept specimen. The evolution of the Laves phase are mainly occurred at the PAGB, or lath and packet boundaries in block-

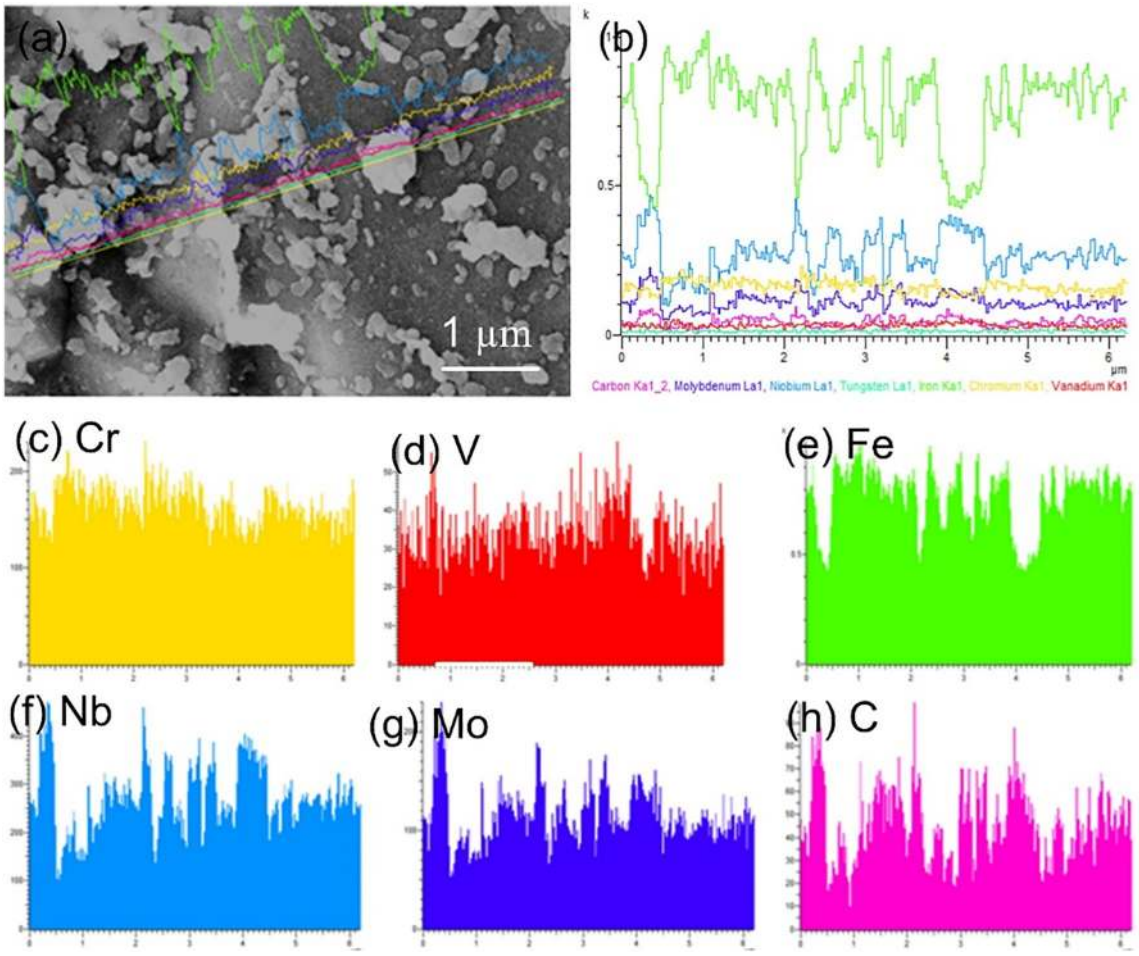

Fig. 6. Line mapping of WFZ in PWNT 1 condition (a) and (b); peaks of different element (c) Cr, (d) V, (e) Fe, (f) Nb, (g) Mo, (h) C.

shape, chain shape, or a bulky shape. The evolution of the Laves phase results in swallowing of the $M_{23}C_6$ and other useful precipitates. That results in degradation of the creep strength of the welds joint.

The formation of the Laves phase is also observed in FGHAZ (point g) and WFZ (point h), respectively. The detailed observation of the coarse Laves phase is also performed using the line and elemental mapping, as discussed below. The size of $M_{23}C_6$ precipitates is measured in a range of 110 to 397 nm, with an average of 283 nm. The size of the Laves phase is measured in a range of 575 to 837 nm, with an average of 695 ± 80 nm.

The crack tip micrograph for PWNT 1 is shown in Fig. 5(a). The EDS analysis(Fig. 5(b))confirms the formation of $M_{23}C_6$ precipitates enriched with Fe and Cr and MX precipitates enriched with Nb. Elemental mapping is performed for the FGHAZ of the crept sample exposed in a high-stress regime of 200 MPa (PWNT 1). The triple point shows the three PAGBs boundaries surrounded by coarse precipitates. The elemental area mapping confirmsthe higher density of C, Nb, and Mo at the PAGBs and poor densityfor Fe. A uniform distribution is observed for the Cr and V. The higher density of C and Mo confirms the formation of the Cr-rich $M_{23}C_6$ phase, and diffusion of Mo precipitates along the boundaries. In as-received conditions, Mo is observed to be distributed both in the matrix region and along the PAGBs; however, a higher weight percentage was observed along the PAGBs [43]. Nb enriched NbC formation is also confirmed along the PAGBs. The Fe shows the poor density at the PAGBs (Fig. 5(c)). Hence, the elemental mapping of FGHAZ confirms the formation of Cr-rich $M_{23}C_6$ and Nb-rich NbX along with the diffusion of Mo towards the PAGBs that latter leads to the nucleation of Laves phase in the expense of $M_{23}C_6$. The elemental line mapping is performed for the WFZ, whichconfirms the higher peak intensity of C, Nb, and Mo at the bulk precipitates while simultaneous lower peak intensity of Fe (Fig. 6). The peaks of the other elements are observed to be uniform except for the Cr. The increase in peaks of Cr at white precipitates confirms the formation of $Cr_{23}C_6$. The higher peak intensity of Mo confirms the accumulation of Mo particles at the PAGBs, and Nb and C confirm the formation of NbC and $Cr_{23}C_6$. The higher peak intensity of Mo might also be due to the evolution of Mo enriched Laves phase. In PWNT 2 condition, the different morphology precipitates at the crack tip are shown in Fig. 7(a) [36]. The detailed characterization of the crack tip has been reported in my previous work [36]. The EDS analysis shows the Nb, C, and Mo as a major element. The area elemental mapping also ensured the segregations of Mo at the PAGBs. The precipitates may be Mo enriched Laves phase, and Mo and Cr enriched $M_{23}C_6$. The higher weight percentage Nb at bulk particles might be due to the formation of NbC at the vicinity of the Laves phase (Fig. 7(c)).

In PWNT 2 condition, to confirm the precipitates in FGHAZ of the crept sample, the detail characterization is reported in Fig. 8. For the same condition, the detailed characterization of the FGHAZ is reported in my previous work [38]. The agglomeration of precipitates along the PAGBs is shown in Fig. 8(a). The EDS analysis of the spectrum (Fig. 8b) ensures the formation of the Mo and W enriched

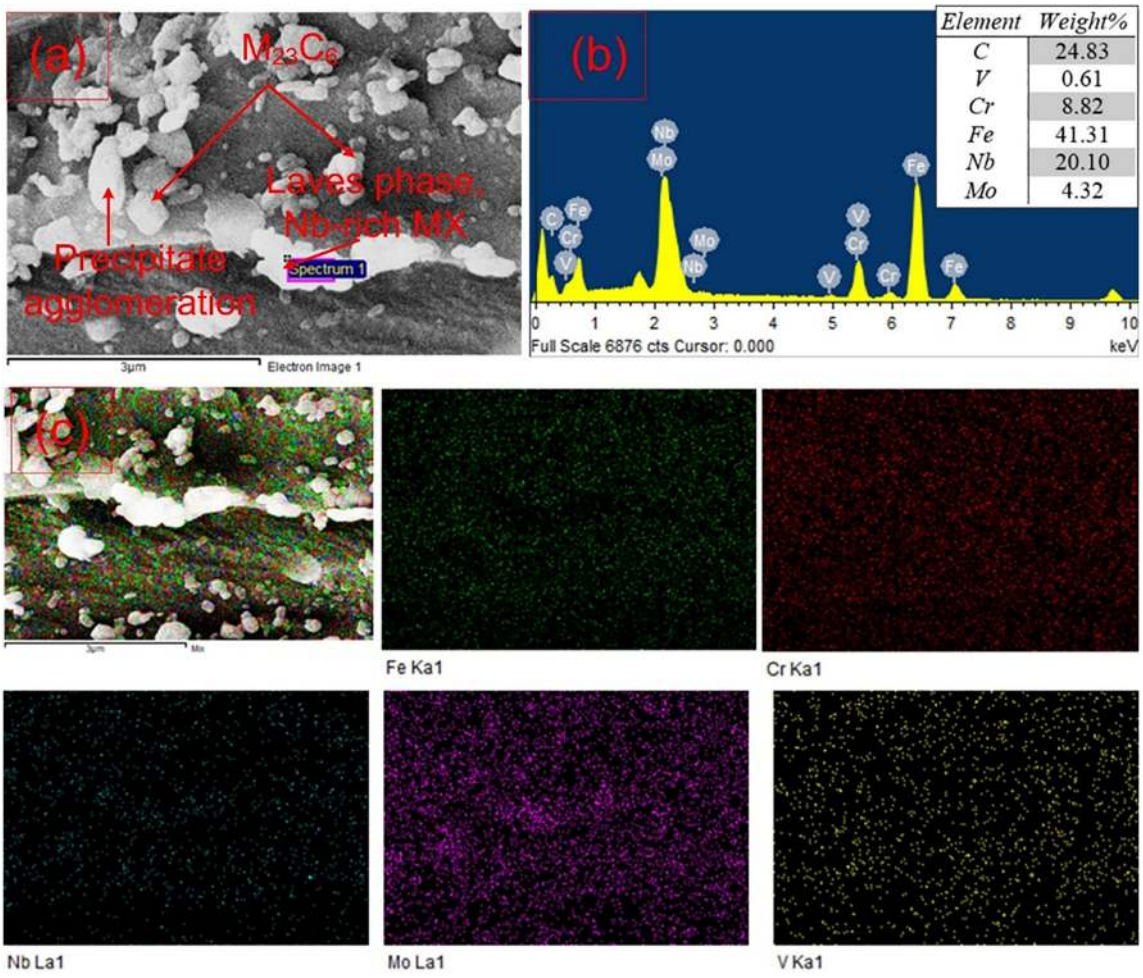

Fig. 7. (a) Crack tip of the crept specimen for PWNT 2 condition, (b) EDS spectra of the white precipitates, (c) area elemental mapping of the crack tip.

Laves phase (Fe_2(W, Mo)). The formation of Nb rich NbX particles is also ensured from the EDS analysis. The elemental line mapping along the boundaries shows the higher peak intensity of Mo and Nb, which also ensures the accumulation of Laves phase and NbX along the PAGBs(Fig. 8(c-d)). Fig. 8(e) shows the results of area elemental mapping. The creep exposure results in the diffusion of Mo from the martensitic matrix to boundaries and surrounds the $M_{23}C_6$ particles. After a certain period of exposure, the higher density of Mo at boundaries leads to the nucleation of the bulky intermetallic Laves phase. The nucleation generally occurs at the $M_{23}C_6$ particles, and after a certain time of exposure formation of the Laves phase results in the swallowing of $M_{23}C_6$ particles and a drastic coarsening rate is observed. From the elemental mapping, a higher density of Mo and Nb is clearly seen on the bulk precipitates. The higher Cr concentration is also observed along with the bulk particles that ensure the surrounding of the Laves phase from the Cr-rich $M_{23}C_6$ particles. The WFZ was characterized for the crept specimen of PWNT 2 and results are depicted in Fig. 9. The EDS analysis confirms the formation of the Laves phase (Fig. 9 (b)). The heterogeneity in the distribution of the Fe, Mo, C, Nb is seen from the area elemental mapping. Mo and Nb show the higher density at the bulk precipitates, which ensures the formation of the Fe_2Mo and NbC. A uniform distribution of V particles inside the martensitic matrix is ensured from Fig. 9(e).

3.2. Microhardness before and after creep tests

The microhardness of the virgin base plate of P91 steel was measured 231 ± 5 HV. In the as-welded condition, a great heterogeneity was reported in hardness along the P91 weldments as a result of the welding heat [44]. The welding heat also leads to the development of the quenching stress in the welds joint, which leads to the premature failure of the welds joint. To remove the quench stresses and enhance the mechanical properties of the welds joint, PWHTs was recommended. PWHT also helps to enhance the creep rupture life of the welds joint by delaying the Type IV failure. However, the hardness gradient still exists across the P91 weldments after the PWHT [12]. The PWNT results in an almost negligible hardness gradient across the P91 weldments, as reported by Pandey et al. [14].

After the creep failure, the variation in hardness along the weldments is shown in Fig. 10. For the low level of the applied stress, the hardness was measured in the range of 190–195 HV at the crack tip. The hardness gets increased as move away from the crack-tip, and the maximum was measured in the WFZ. The hardness in WFZ and HAZ does not show much variation after the creep failure. Sample crept in high applied stress regime shows the higher hardness as compared to sample crept in low-stress regimes of 150 MPa. The hardness near the crack tip is measured to be 215 HV (PWNT 1)

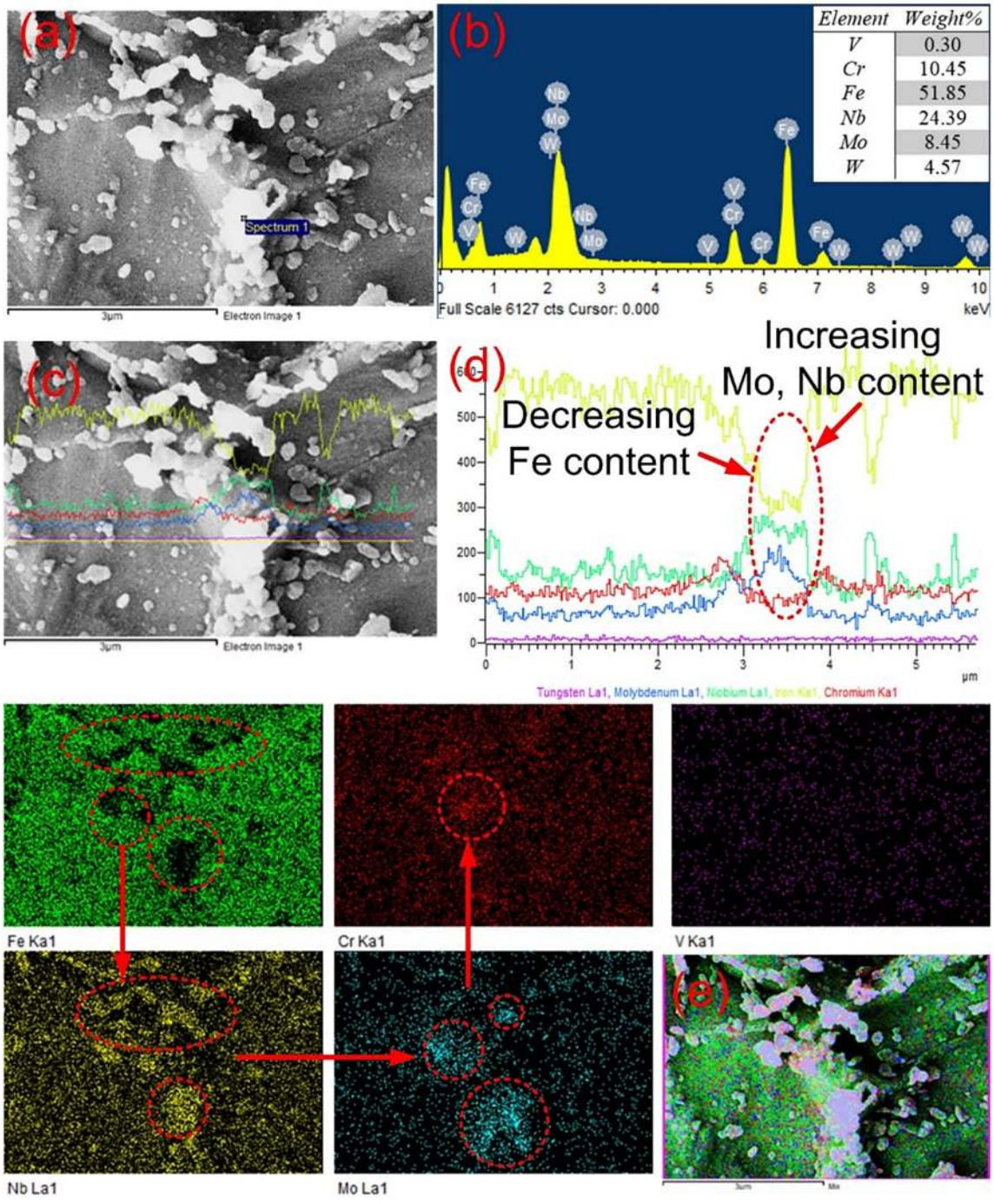

Fig. 8. For PWNT 2: (a) SE micrograph of FGHAZ showing the formation of Laves phase, (b) EDS spectra of white particles, (c) and (d) elemental line mapping at PAGBs, (e) elemental area mapping of the microstructure.

and observed to be decreased as the move away towards the WFZ. The hardness measured in FGHAZ is higher for the PWNT 1 as compared to PWNT 2. However, the average hardness measured in the WFZ was 203 HV for both PWNT 1 and PWNT 2. As compared to the PWNT sample before the creep exposure, a slight decrease in hardness of P91 weldments was observed after the creep rupture.

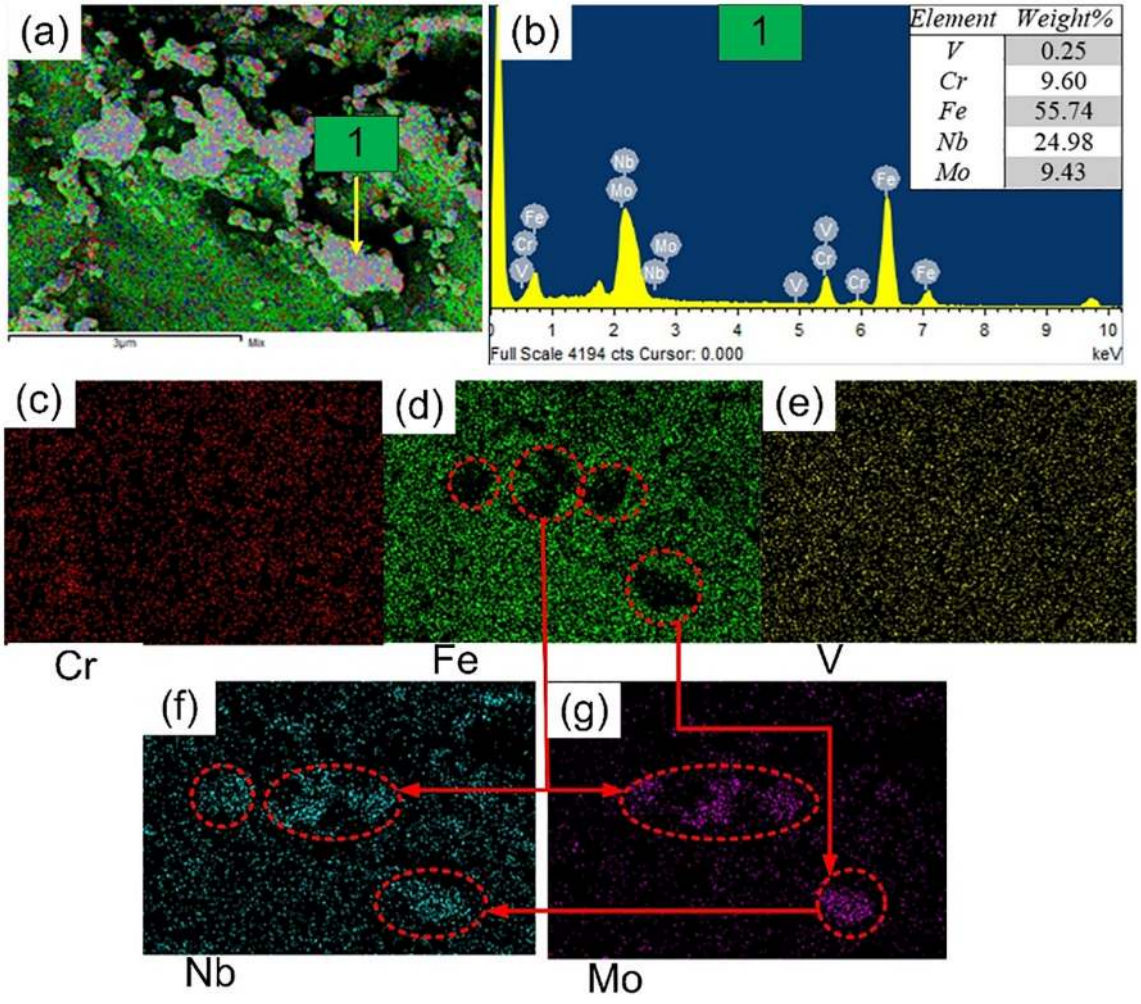

Fig. 9. For PWNT 2: (a) SE micrograph of WFZ with elemental mapping, (b) EDS spectra of precipitates, elemental mapping showing distribution of the: (c) Cr, (d)Fe, (e)V, (f) Nb, (g) Mo [34].

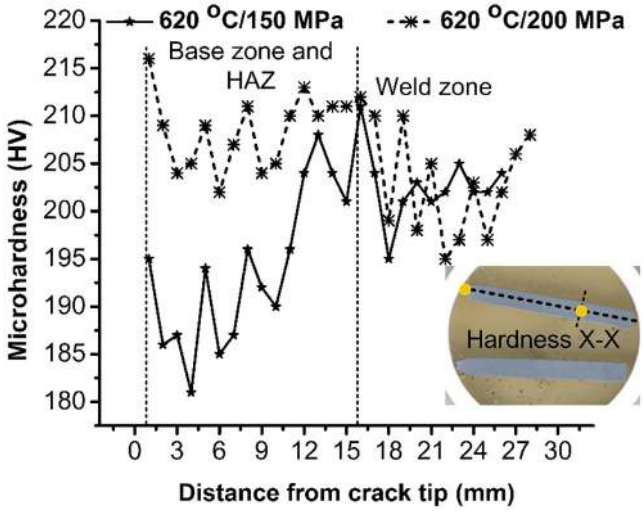

Fig. 10. Hardness variation along the weldments in the crept sample [28].

4. Conclusions

The present research work showed the effect of the heat-treatment on creep rupture behavior of the P91 welds joint. The obtained results have been summarized as follows:

- The crept sample at high applied stress regime (PWNT 1) showed the coarsening of $M_{23}C_6$ precipitates along with the diffusion of Mo towards thePAGBs for each region of the weldments (crack tip, FGHAZ, and WFZ).
- The crept sample at a low applied stress regime (PWNT 2) showed the nucleation of the Mo-enrichedinter-metallic Laves phase at the grain boundaries in the expense of $M_{23}C_6$ for each zone of the weldments. The segregation of the Nb particles at the PAGBs has also been observed.
- A higher density of creep voids was observed at the triple boundaries, which was associated with a higher density of coarse $M_{23}C_6$ precipitates. The interface of the brittle phases (coarse $M_{23}C_6$ precipitatesand Laves phase)and soft matrix at the triple boundaries led tohigher stress concentration that resulted inthe formation of and creep voids.

CRediT authorship contribution statement

S. Kumar: Data curation, Formal analysis, Methodology, Writing - original draft. **S. Sirohi:** Validation. **J.G. Thakare Surpervision:** . **B. Adhithan:** Validation. **C. Pandey:** Supervision, Validation, Visualization, Writing - review & editing.

Declaration of Competing Interest

The authors declare that they have no known competing financial interests or personal relationships that could have appeared to influence the work reported in this paper.

References

[1] B. Xiao, L. Xu, L. Zhao, H. Jing, Y. Han, Z. Tang, Microstructure evolution and fracture mechanism of a novel 9Cr tempered martensite ferritic steel during short-term creep, Mater. Sci. Eng. A. 707 (2017) 466–477, https://doi.org/10.1016/j.msea.2017.09.086.

[2] R.N. Hajra, A.K. Rai, H.P. Tripathy, S. Raju, S. Saroja, Influence of tungsten on transformation characteristics in P92 ferritic–martensitic steel, J. Alloys Compd. 689 (2016) 829–836, https://doi.org/10.1016/j.jallcom.2016.08.055.

[3] K. Kimura, H. Kushima, K. Sawada, Long-term creep deformation property of modified 9Cr-1Mo steel, Mater. Sci. Eng. A. 510–511 (2009) 58–63, https://doi.org/10.1016/j.msea.2008.04.095.

[4] C. Pandey, N. Saini, M.M. Mahapatra, P. Kumar, Study of the fracture surface morphology of impact and tensile tested cast and forged (C&F) Grade 91 steel at room temperature for different heat treatment regimes, Eng. Fail. Anal. 71 (2016) 131–147, https://doi.org/10.1016/j.engfailanal.2016.06.012.

[5] C. Pandey, M.M. Mahapatra, P. Kumar, N. Saini, Effect of strain rate and notch geometry on tensile properties and fracture mechanism of creep strength enhanced ferritic P91 steel, J. Nucl. Mater. 498 (2018) 176–186, https://doi.org/10.1016/j.jnucmat.2017.10.037.

[6] L. Maddi, G.S. Deshmukh, A.R. Ballal, D.R. Peshwe, R.K. Paretkar, K. Laha, M.D. Mathew, Effect of Laves phase on the creep rupture properties of P92 steel, Mater. Sci. Eng. A. 668 (2016) 215–223, https://doi.org/10.1016/j.msea.2016.05.074.

[7] C. Schroer, J. Konys, T. Furukawa, K. Aoto, Oxidation behaviour of P122 and a 9Cr-2W ODS steel at 550 °C in oxygen-containing flowing lead-bismuth eutectic, J. Nucl. Mater. 398 (2010) 109–115, https://doi.org/10.1016/j.jnucmat.2009.10.019.

[8] C. Pandey, M.M. Mahapatra, Effect of heat treatment on microstructure and hot Impact toughness of various zones of P91 welded pipes, J. Mater. Eng. Perform. 25 (2016) 2195–2210, https://doi.org/10.1007/s11665-016-2064-x.

[9] C. Pandey, M.M. Mahapatra, P. Kumar, N. Saini, Effect of normalization and tempering on microstructure and mechanical properties of V-groove and narrow-groove P91 pipe weldments, Mater. Sci. Eng. A. 685 (2017) 39–49, https://doi.org/10.1016/j.msea.2016.12.079.

[10] S. Sirohi, C. Pandey, A. Goyal, Characterization of structure-property relationship of martensitic P91 and high alloy ferritic austenitic F69 steel, Int. J. Press. Vessel. Pip. (2020), https://doi.org/10.1016/j.ijpvp.2020.104179 104179.

[11] C. Pandey, M.M. Mahapatra, P. Kumar, N. Saini, Homogenization of P91 weldments using varying normalizing and tempering treatment, Mater. Sci. Eng. A. 710 (2018) 86–101, https://doi.org/10.1016/j.msea.2017.10.086.

[12] C. Pandey, M.M. Mahapatra, Effect of groove design and post-weld heat treatment on microstructure and mechanical properties of P91 steel weld, J. Mater. Eng. Perform. 25 (2016) 2761–2775, https://doi.org/10.1007/s11665-016-2127-z.

[13] C. Pandey, M.M. Mahapatra, P. Kumar, A comparative study of transverse shrinkage stresses and residual stresses in P91 welded pipe including plasticity error, Arch. Civ. Mech. Eng. 18 (2018) 1000–1011, https://doi.org/10.1016/j.acme.2018.02.007.

[14] C. Pandey, M.M. Mahapatra, P. Kumar, N. Saini, A. Srivastava, Microstructure and mechanical property relationship for different heat treatment and hydrogen level in multi-pass welded P91 steel joint, J. Manuf. Process. 28 (2017) 220–234, https://doi.org/10.1016/j.jmapro.2017.06.009.

[15] V.L. Manugula, K.V. Rajulapati, G. Madhusudhan Reddy, K. Bhanu, S. Rao, Role of evolving microstructure on the mechanical properties of electron beam welded ferritic-martensitic steel in the as-welded and post weld heat- treated states, Mater. Sci. Eng. A. 698 (2017) 36–45, https://doi.org/10.1016/j.msea.2017.05.036.

[16] K. Sawada, M. Bauer, F. Kauffmann, P. Mayr, A. Klenk, Microstructural change of 9% Cr-welded joints after long-term creep, Mater. Sci. Eng. A. 527 (2010) 1417–1426, https://doi.org/10.1016/j.msea.2009.10.044.

[17] Y. Tsuchida, K. Okamoto, Y. Tokunaga, Study of creep rupture strength in heat affected zone of 9Cr-1Mo-V-Nb-N steel by welding thermal cycle simulation, Weld. Int. 10 (1996) 454–460, https://doi.org/10.1080/09507119609549030.

[18] C. Pandey, M.M. Mahapatra, P. Kumar, N. Saini, Some studies on P91 steel and their weldments, J. Alloys Compd. 743 (2018) 332–364, https://doi.org/10.1016/j.jallcom.2018.01.120.

[19] Y. Wang, L. Li, Microstructure evolution of fine grained heat affected zone in type IV failure of P91 welds, Weld. J. 95 (2016) 27–36. http://s3.amazonaws.com/WJ-www.aws.org/supplement/WJ_2016_01_s27.pdf%5Cnhttps://drive.google.com/open?id=0B0fTxDBXtHZMaVZwMzNRT0piTXc.

[20] S.K. Albert, M. Tabuchi, H. Hongo, T. Watanabe, K. Kubo, M. Matsui, Effect of welding process and groove angle on type IV cracking behaviour of weld joints of a ferritic steel, Sci. Technol. Weld. Join. 10 (2005) 149–157, https://doi.org/10.1179/174329305X36034.

[21] M. Divya, C.R. Das, S.K. Albert, S. Goyal, P. Ganesh, R. Kaul, J. Swaminathan, B.S. Murty, L.M. Kukreja, A.K. Bhaduri, Influence of welding process on Type IV cracking behavior of P91 steel, Mater. Sci. Eng. A. 613 (2014) 148–158, https://doi.org/10.1016/j.msea.2014.06.089.

[22] H. Hongo, M. Tabuchi, T. Watanabe, Type IV creep damage behavior in Gr.91 steel welded joints, Metall. Mater. Trans. A Phys. Metall. Mater. Sci. 43 (2012) 1163–1173, https://doi.org/10.1007/s11661-011-0967-6.

[23] S.K. Albert, M. Matsui, T. Watanabe, H. Hongo, K. Kubo, M. Tabuchi, Variation in the type IV cracking behaviour of a high Cr steel weld with post weld heat treatment, Int. J. Press. Vessel. Pip. 80 (2003) 405–413, https://doi.org/10.1016/S0308-0161(03)00072-3.

[24] J.A. Francis, G.M.D. Cantin, W. Mazur, H.K.D.H. Bhadeshia, Effects of weld preheat temperature and heat input on type IV failure, Sci. Technol. Weld. Join. 14 (2009) 436–442, https://doi.org/10.1179/136217109X415884.

[25] M. Abd El-Rahman Abd El-Salam, I. El-Mahallawi, M.R. El-Koussy, Influence of heat input and post-weld heat treatment on boiler steel P91 (9Cr – 1Mo – V – Nb) weld joints Part 2 – Mechanical properties, Int. Heat Treat. Surf. Eng. 7 (2013) 32–37.

[26] C. Pandey, M.M. Mahapatra, P. Kumar, F. Daniel, B. Adhithan, Softening mechanism of P91 steel weldments using heat treatments, Arch. Civ. Mech. Eng. 19 (2019) 297–310, https://doi.org/10.1016/j.acme.2018.10.005.

[27] C. Pandey, Mechanical and metallurgical characterization of dissimilar P92/SS304 L welded joints under varying heat treatment regimes, Metall. Mater. Trans. A. 51 (2020) 2126–2142, https://doi.org/10.1007/s11661-020-05660-0.

[28] C. Pandey, M. Mohan Mahapatra, P. Kumar, J.G. Thakre, N. Saini, Role of evolving microstructure on the mechanical behaviour of P92 steel welded joint in as-welded and post weld heat treated state, J. Mater. Process. Technol. 263 (2019) 241–255. https://doi.org/10.1016/j.jmatprotec.2018.08.032.

[29] S. Kumar, C. Pandey, A. Goyal, Role of dissimilar IN617 nickel alloy consumable on microstructural and mechanical behavior of P91 welds joint, Arch. Civ. Mech. Eng. (2020), https://doi.org/10.1007/s43452-020-00104-3.

[30] T. Schaupp, W. Ernst, H. Spindler, T. Kannengiesser, Hydrogen-assisted cracking of GMA welded 960 MPa grade high-strength steels, Int. J. Hydrogen Energy. 45 (2020) 20080–20093, https://doi.org/10.1016/j.ijhydene.2020.05.077.

[31] J. Tomków, D. Fydrych, G. Rogalski, Role of bead sequence in underwater welding, Materials (Basel). 12 (2019) 1–10, https://doi.org/10.3390/ma12203372.

[32] C. Pandey, N. Saini, M.M. Mahapatra, P. Kumar, Hydrogen induced cold cracking of creep resistant ferritic P91 steel for different diffusible hydrogen levels in deposited metal, Int. J. Hydrogen Energy. 41 (2016) 17695–17712, https://doi.org/10.1016/j.ijhydene.2016.07.202.

[33] C. Pandey, M.M. Mahapatra, P. Kumar, N. Saini, Diffusible hydrogen level in deposited metal and their effect on tensile properties and flexural strength of P91 steel, J. Eng. Mater. Technol. 139 (2017) 1–11, https://doi.org/10.1115/1.4035764.

[34] C. Pandey, M.M. Mahapatra, P. Kumar, S. Kumar, Effect of post weld heat treatments on microstructure evolution and type IV cracking behavior of the P91 steel welds joint, J. Mater. Process. Technol. 266 (2019) 140–154, https://doi.org/10.1016/j.jmatprotec.2018.10.024.

[35] C. Pandey, M. Mahapatra, Evolution of phases during tempering of P91 steel at 760 for varying tempering time and their effect on microstructure and mechanical properties, Proc. Inst. Mech. Eng. Part E J. Process Mech. Eng. 664 (2016) 58–74, https://doi.org/10.1177/0954408916656678.

[36] C. Pandey, M.M. Mahapatra, P. Kumar, Effect of post weld heat treatments on fracture frontier and type IV cracking nature of the crept P91 welded sample, Mater. Sci. Eng. A. 731 (2018) 249–265, https://doi.org/10.1016/j.msea.2018.06.038.

[37] C. Pandey, M.M. Mahapatra, P. Kumar, A. Giri, Microstructure characterization and Charpy toughness of P91 weldment for as-Welded, post-weld heat treatment and normalizing & tempering heat treatment, Met. Mater. Int. 23 (2017) 900–914, https://doi.org/10.1007/s12540-017-6850-2.

[38] C. Pandey, The characterization of soft fine-grained heat-affected zones in P91 weldments under creep exposure conditions, Steel Res. Int. 91 (2020) 1–8, https://doi.org/10.1002/srin.201900342.

[39] L. Korcakova, J. Hald, M.A.J. Somers, Quantification of laves phase particle size in 9CrW steel, Mater. Charact. 47 (2001) 111–117, https://doi.org/10.1016/S1044-5803(01)00159-0.

[40] A. Aghajani, F. Richter, C. Somsen, S.G. Fries, I. Steinbach, G. Eggeler, On the formation and growth of Mo-rich Laves phase particles during long-term creep of a 12% chromium tempered martensite ferritic steel, Scr. Mater. 61 (2009) 1068–1071, https://doi.org/10.1016/j.scriptamat.2009.08.031.

[41] K. Laha, K.S. Chandravathi, P. Parameswaran, K.B.S. Rao, S.L. Mannan, Characterization of microstructures across the heat-affected zone of the modified 9Cr-1Mo weld joint to understand its role in promoting type IV cracking, Metall. Mater. Trans. A. 38 (2007) 58–68, https://doi.org/10.1007/s11661-006-9050-0.

[42] C.G. Panait, A. Zielinska-Lipiec, T. Koziel, A. Czyrska-filemonowicz, A.F. Gourgues-Lorenzon, W. Bendick, Evolution of dislocation density, size of

subgrains and MX-type precipitates in a P91 steel during creep and during thermal ageing at 600 oC for more than 100,000h, Mater. Sci. Eng. A. 527 (2010) 4062–4069, https://doi.org/10.1016/j.msea.2010.03.010.

[43] C. Pandey, M.M. Mahapatra, P. Kumar, R.S. Vidyrathy, A. Srivastava, Microstructure-based assessment of creep rupture behaviour of cast-forged, Mater. Sci. Eng. A. 695 (2017) 291–301, https://doi.org/10.1016/j.msea.2017.04.037.

[44] C. Pandey, H.K. Narang, N. Saini, M.M. Mahapatra, P. Kumar, Microstructure and transverse shrinkage stress analysis in GTA welds of P91 steel pipe, Int. J. Steel Struct. 17 (2017), https://doi.org/10.1007/s13296-017-6030-8.